

# Advantages of Estimating Rate Corrections During Dynamic Propagation of Spacecraft Rates—Applications to Real-Time Attitude Determination of SAMPEX\*

M. S. Challa and G. A. Natanson  
Computer Sciences Corporation (CSC)  
Lanham-Seabrook, Maryland

D. F. Baker and J. K. Deutschmann  
Goddard Space Flight Center (GSFC)  
Greenbelt, Maryland

## Abstract

This paper describes real-time attitude determination results for the Solar, Anomalous, and Magnetospheric Particle Explorer (SAMPEX), a gyroless spacecraft, using a Kalman filter/Euler equation approach denoted the Real-Time Sequential Filter (RTSF). The RTSF is an extended Kalman filter whose state vector includes the attitude quaternion and corrections to the rates, which are modeled as Markov processes with small time constants. The rate corrections impart a significant robustness to the RTSF against errors in modeling the environmental and control torques, as well as errors in the initial attitude and rates, while maintaining a small state vector.

SAMPEX flight data from various mission phases are used to demonstrate the robustness of the RTSF against a priori attitude and rate errors of up to 90 deg and 0.5 deg/sec, respectively, as well as a sensitivity of 0.0003 deg/sec in estimating rate corrections in torque computations. In contrast, it is shown that the RTSF attitude estimates without the rate corrections can degrade rapidly. RTSF advantages over single-frame attitude determination algorithms are also demonstrated through (1) substantial improvements in attitude solutions during Sun-magnetic field coalignment and (2) magnetic-field-only attitude and rate estimation during the spacecraft's Sun-acquisition mode.

A robust magnetometer-only attitude-and-rate determination method is also developed to provide for the contingency when both Sun data as well as a priori knowledge of the spacecraft state are unavailable. This method includes a deterministic algorithm used to initialize the RTSF with coarse estimates of the spacecraft attitude and rates. The combined algorithm has been found effective, yielding accuracies of 1.5 deg in attitude and 0.01 deg/sec in the rates and convergence times as little as 400 sec.

## 1. Introduction

A crucial aspect of an attitude Kalman filter is that the attitude quaternion  $q$  and the covariance matrix must be propagated between measurements using the spacecraft's angular velocity (also referred to here as the rates),  $\omega$ . Thus,  $q$  is propagated via

$$\frac{dq}{dt} = \frac{1}{2} \mathbf{\Omega}(\omega) q \quad (1)$$

where

$$\mathbf{\Omega}(\omega) = \begin{bmatrix} -[\omega \times] & \omega \\ -\omega^T & 0 \end{bmatrix} \quad (2)$$

and  $\omega_x$ ,  $\omega_y$ , and  $\omega_z$  are the components of  $\omega$  along the spacecraft's body axes. Note that matrices, including vectors (column matrices), are denoted in boldface in this paper, matrix transposes are denoted by the superscript  $T$ , and

---

\*This work was supported by the National Aeronautics and Space Administration (NASA)/Goddard Space Flight Center (GSFC), Greenbelt, Maryland, under Contract NAS 5-31500.

$$[\omega \times] = \begin{bmatrix} 0 & -\omega_z & \omega_y \\ \omega_z & 0 & -\omega_x \\ -\omega_y & \omega_x & 0 \end{bmatrix} \quad (3)$$

Equation (3) defines a cross product-to-matrix equivalence that will be used elsewhere in this paper. Attitude here denotes the orientation of the spacecraft body frame with respect to the geocentric inertial frame (GCI),  $\omega$  describes the rate of change of the attitude, and all vectors are resolved along the body axes unless specified otherwise.

For a gyro-based spacecraft, gyros accurately measure  $\omega$ , and accurate results can be obtained by integrating Equation (1) alone. For a gyroless spacecraft such as the Solar, Anomalous, and Magnetospheric Particle Explorer (SAMPEX), however, we must propagate the rates via the following Euler equation (References 1 and 2):

$$\frac{dL}{dt} = N_{tot} - \omega \times L \quad (4)$$

where  $N_{tot}$  is the sum of the external torques acting on the spacecraft, and  $L$  is the total angular momentum of the spacecraft. If  $I$  is the inertia tensor of the rigid part of the spacecraft and  $h$  denotes angular momentum contribution from rotating parts such as momentum wheels,  $L$  is given by

$$L = I\omega + h \quad (5)$$

Equations (1) and (4) generally pose a difficult initial-value problem, because significant errors in  $\omega$  can arise from spacecraft and torque models, as well as the initial values of  $q$  and  $\omega$  used in the integration.

Of course, we may avoid rate propagation altogether by using only single-frame algorithms such as TRIAD (algebraic method in Reference 1) and QUEST (Reference 3), which determine the attitude using at least two simultaneous measurements. But these methods do not provide accurate solutions when all of the observed vectors are nearly collinear. A Kalman filter is superior in such a situation, as will be demonstrated later, since it can use propagation to estimate the unobservable elements of the state. Additionally, modeling the spacecraft's dynamics is advantageous because it accounts for other physical phenomena such as nutational frequencies.

A Kalman filter scheme that corrects for the errors in  $\omega$  is thus desirable. This paper presents results from such a filter developed for the PC-based SAMPEX real-time attitude determination system (Reference 4), denoted the Real-Time Sequential Filter (RTSF). Only pertinent aspects of the SAMPEX RTSF are discussed here; complete details, including system aspects, mathematics, and models for the environmental torques, are given in References 5-7.

The basic features of the SAMPEX RTSF are as follows. Let  $\omega_{prop}$  denote the rates generated through Equation (4), and let  $\omega_{true}$  denote the true rates. The errors are the difference of the two, and these errors are modeled as being of two types: a zero-mean white noise vector,  $\eta_\omega$ , and a systematic error,  $b_{true}$ , i.e.,

$$\omega_{prop} = \omega_{true} + b_{true} + \eta_\omega \quad (6)$$

In addition to the quaternion, we wish to estimate the rate errors  $b$  using the following Kalman state vector:

$$X = [q^T \ b^T]^T \quad (7)$$

together with the following general principles:

- Model  $N_{tot}$  as accurately as possible.
- Model noise terms such as  $\eta_\omega$  by treating them as a noisy background arising from torque uncertainties and accounting for them statistically in the Kalman filter formulation.
- Estimate  $b$  optimally by using the sensor residuals, and propagate  $b$  between measurements using a suitable dynamics model.

To formulate a dynamics model for  $b$ , we first note the following aspect of Equation (4): It is not reasonable to treat  $b$  as constant because even constant errors in  $N_{tot}$  do not necessarily generate constant  $b$ . In fact, in view of the sporadic nature of the control torques as well as the attitude dependence of the environmental torques, it is uncertain whether a simple dynamic model can be developed for  $b$ . We avoid this issue by arguing that we are interested not in the origin of  $b$ , but in its instantaneous value that would reconcile the differences between the propagated and observed

values of  $q$ . Consider now propagation between measurement times  $t_k$  and  $t_{k+1}$  and use the following notation: filter estimates are denoted by carets; estimates before and after updates (via measurements) are denoted by minus signs and plus signs, respectively; and the times are denoted by subscripts  $k$  and  $k+1$ . In this notation,  $\hat{\omega}_k(-) \equiv \omega_{prop}(t_k)$ , and we seek to correct the rates using

$$\hat{\omega}_k(+) = \hat{\omega}_k(-) - \hat{b}_k(+) \quad (8)$$

Propagation of  $q$ ,  $\omega$ , and the covariance matrix,  $P$ , to  $t_{k+1}$  is then done using  $\hat{\omega}_k(+)$ . Since Equation (8) corrects the rates at  $t_k$ , it follows that  $\hat{b}_{k+1}(+)$  must reflect only errors that accumulated during the intervening period,  $\Delta t = t_{k+1} - t_k$ .

Kalman filter updates, however, are of the form:

$$\hat{b}_{k+1}(+) = \hat{b}_{k+1}(-) + \Delta b_{k+1}^* \quad (9)$$

where  $\Delta b_{k+1}^*$  denotes the correction estimated by the filter. It follows that  $\hat{b}_{k+1}(+)$  (and  $\Delta b_{k+1}^*$ ) will denote the errors in  $\hat{\omega}_{k+1}(-)$  if  $\hat{b}_{k+1}(-) \approx 0$ . This is achieved in the RTSF by specifying that  $\hat{b}$  decays exponentially with a time constant,  $\tau$ , of the order of  $\Delta t$ . That is, we model the dynamics of  $\hat{b}$  through the first-order Markov model:

$$\frac{d\hat{b}}{dt} = -\tau^{-1}\hat{b} + \eta_b \quad (10)$$

where  $\eta_b$  is another zero-mean white noise vector.

The above Markov model also assists in tuning the filter through the following useful feature: The diagonal elements of  $P$  corresponding to  $\hat{b}$  would then converge to a constant value that depends on  $\tau$  and the statistical properties of  $\eta_b$ . For simplicity, take  $\hat{b}$  and  $\eta_b$  as scalars, and define  $Q$ , through  $\langle \eta_b(t) \eta_b(t')^T \rangle = Q(t) \delta(t-t')$ , where  $\delta(t-t')$  is the Dirac delta function. Then  $p_{..}$ , the Kalman filter's covariance matrix element for  $\hat{b}$ , converges to  $p_{..}$  given by

$$p_{..} = Q\tau/2 \quad (11)$$

Let us now suppose that the  $\langle |\eta_b|^2 \rangle$  is known by examining the model uncertainties in Equation (4). We argue that  $p_{..}$  is also of this order of magnitude since  $\hat{b}$  cannot be known to a greater degree of precision than  $\omega$  itself. Thus, we use  $p_{..}$  and  $\tau$  together to fix the numerical value of  $Q$  in Equation (11), and then use  $Q$  in the Kalman filter computations.

This formulation for estimating  $\hat{b}$  has many similarities to gyro-bias estimation (References 8-10), where  $\hat{b}$  denotes the gyro drift-rate biases and  $\hat{\omega}(-)$  denotes uncorrected gyro rates. In view of the slow variation of these biases over time (see, e.g., Reference 11), it is then possible to approximate their dynamics by Equation (10) using a *large* value for  $\tau$ . There is one important difference, though, between the two situations. Gyros accurately measure  $\omega$ , and the leading errors in the gyro rates are indeed removed by estimating essentially constant biases. Thus, for example,  $\hat{b}_k(+)$  is subtracted from *both*  $\hat{\omega}_k(-)$  and  $\hat{\omega}_{k+1}(-)$  and before their mean is used to propagate  $q$  via Equation (1). Consequently, the increments,  $\Delta \hat{b}$ , to  $\hat{b}$  provided by the Kalman updates take  $\hat{b}$  progressively closer to that constant.

The rest of this paper is organized as follows. Sections 2 and 3 summarize details of the spacecraft, the data used here, and the theory. Sections 4 and 5 are devoted to tuning, accuracy, and robustness of the filter. Section 6 demonstrates the advantages of the RTSF over single-frame solutions by (1) showing its stability when Sun and magnetic field vectors are nearly parallel and (2) determining attitude and rates using only magnetic field data. Section 7 shows that combining the RTSF with the deterministic algorithm of References 12 and 13 yields a robust magnetometer-only attitude-and-rate determination scheme. Section 8 summarizes the conclusions.

## 2. Description of SAMPEX and Data Characteristics

SAMPEX is the first of the Small Explorer satellites and is designed to study elemental and isotopic composition of energetic particles of solar and cosmic origin. It has a 550x675 km orbit with an 82-deg inclination. SAMPEX nominally is Sun-pointing and has a rate of 1 rotation per orbit (RPO) about the spacecraft-to-Sun vector. The attitude accuracy

requirement of 2 deg is achieved using a fine Sun sensor (FSS) and a three-axis magnetometer (TAM). The control hardware consists of a momentum wheel and a magnetic torquer assembly (MTA).

The nominal body  $y$ -axis is the Sun vector, and the nominal  $x$ - and  $z$ -body axes are defined by the Sun/orbital frame of Reference 14. For our purposes, it suffices to note the following:

- The body  $y$ -axis is the pitch axis and also the FSS boresight, and the angular deviations of this axis from the Sun vector are defined as the roll and yaw angles, which are measured by the FSS.
- The pitch angle denotes angular errors about the  $y$ -axis and is measured by the TAM.
- Pitch control is derived through the wheel whose axis coincides with the body  $y$ -axis, whereas the MTA primarily provides roll and yaw control, and angular momentum dumping.
- During the nominal 1-RPO mode, roll, pitch, and yaw angles are all 0, and  $\omega \approx (0, 0.06, 0)$  deg/sec.

SAMPEX telemetry datasets of Table 1 are used here and, with the exception of SIM722, they all contain inflight data. SIM722 was constructed (Reference 7) using SAMPEX ephemerides and the wheel data from PB722 and is useful in calibrating the accuracy of the  $b$  estimates.

**Table 1. Highlights of the SAMPEX Telemetry Datasets Used for Evaluating the RTSF**

Name of Dataset	Features
PB705	Transition from Sun-acquisition mode to nominal 1-RPO mode on the day of launch, 7/4/92
PASS53	Nominal 1-RPO mode data of 7/8/92
SIM722	Simulated data for duration of eclipse (Earth shadow) on 7/21/92
PB825	Near-coalignment of Sun and magnetic field vectors on 8/23/92
PB722	Inflight data for the eclipse of SIM722

No significant differences were noticed between QUEST and TRIAD attitude solutions. The TRIAD attitude solutions were differenced to provide rates, and the single-frame results are often taken as the truth models accurate to: 0.5 deg for roll/yaw, 1.5 deg for pitch, and 0.5 deg/sec for rates.

### 3. Theoretical Aspects of the RTSF

#### Definition of Errors:

The Kalman filter formalism here follows the scheme of Reference 15; i.e., state errors before and after an update are considered, and the differential equation for  $P$  is derived by demanding optimality. The following notation is used in addition to that in Section 1.  $A$  generally denote an orthogonal matrix;  $A(q)$  is then the orthogonal matrix parameterized by a quaternion  $q$ . Quaternion multiplication, denoted by  $\otimes$ , is defined here in the reverse order of the corresponding attitude matrices; i.e.,  $q = q_1 \otimes q_2$  is equivalent to  $A(q) = A(q_2)A(q_1)$ .

The attitude error is linearized, and is taken as a vector of three small independent Euler angles,  $\alpha = (\alpha_x, \alpha_y, \alpha_z)$ , needed to rotate the true body frame onto the estimated body frame. That is, if

$$\delta q \approx \begin{bmatrix} \alpha^T \\ 2 & 1 \end{bmatrix}^T \quad (12)$$

then  $A(\hat{q}) = A(\delta q)A(q_{true})$ . The error  $x$  in the state vector  $X$  of Equation (7) is then

$$x = [\alpha^T \quad \Delta b^T]^T \quad (13)$$

The 6x6 covariance matrix  $\mathbf{P}$  is then defined as  $\mathbf{P} = \langle \mathbf{x} \mathbf{x}^T \rangle$ . If  $\mathbf{X}_{true} = [\mathbf{q}_{true}^T \ \mathbf{b}_{true}^T]^T$  is the true state vector, the following relationships hold:

$$\hat{\mathbf{q}}(\pm) = \mathbf{q}_{true} \otimes \delta \mathbf{q}(\pm) \quad (14)$$

$$\hat{\mathbf{b}}(\pm) = \mathbf{b}_{true} - \Delta \mathbf{b}(\pm)$$

The sign convention for  $\Delta \mathbf{b}$  ensures that, from Equations (6) and (8), the rate estimates are of the following form:

$$\hat{\boldsymbol{\omega}} = \boldsymbol{\omega}_{true} + \Delta \mathbf{b} + \boldsymbol{\eta}_{\omega} \quad (15)$$

Let

$$\mathbf{x}^* = [\boldsymbol{\alpha}^{*T} \ \Delta \mathbf{b}^{*T}]^T \quad (16)$$

be the errors estimated by the filter.  $\hat{\mathbf{X}}$  is then updated through

$$\hat{\mathbf{q}}(+)=\hat{\mathbf{q}}(-)\otimes(\delta \mathbf{q})^{-1} \quad (17)$$

$$\hat{\mathbf{b}}(+)=\hat{\mathbf{b}}(-)+\Delta \mathbf{b}^*$$

The relation between the state errors before and after an update follows as  $\mathbf{x}(+) = \mathbf{x}(-) - \mathbf{x}^*$ .

### Propagation From $t_k$ to $t_{k+1}$ :

$\hat{\mathbf{b}}$  is propagated readily after ignoring  $\boldsymbol{\eta}_b$  in Equation (9), i.e.,

$$\hat{\mathbf{b}}_{k+1}(-) = \hat{\mathbf{b}}_k(+) \exp\left[-\left(\frac{t_{k+1}-t_k}{\tau}\right)\right]$$

Regarding the rates,  $\hat{\boldsymbol{\omega}}$  is first updated via Equation (8), and  $\hat{\mathbf{L}}$  is updated using Equation (5):  $\hat{\mathbf{L}}_k(+)=\mathbf{I} \hat{\boldsymbol{\omega}}_k(+)+\mathbf{h}_k$ . Here  $\mathbf{h}$  is the wheel momentum given by  $\mathbf{h}=[0 \ I_{whl} \omega_{whl} \ 0]^T$ , where  $I_{whl}$  is the moment of inertia of the wheel about its axis and  $\omega_{whl}$  is the wheel speed.  $\hat{\boldsymbol{\omega}}_k(+)$  and  $\hat{\mathbf{L}}_k(+)$  are then used to numerically integrate Equations (1) and (4) to obtain  $\hat{\mathbf{q}}_{k+1}(-)$  and  $\hat{\mathbf{L}}_{k+1}(-)$ , along with the differential equation for  $\mathbf{P}$  to be given shortly. The uncorrected rates at  $t_{k+1}$  are then obtained by inverting Equation (5), i.e.,  $\hat{\boldsymbol{\omega}}_{k+1}(-)=\mathbf{I}^{-1}[\hat{\mathbf{L}}_{k+1}(-)-\mathbf{h}_{k+1}]$ .

While propagating  $\hat{\mathbf{L}}$ ,  $N_{tor}$  is modeled as the sum of four external torques: magnetic control ( $N_{mag}$ ), gravity gradient, aerodynamic, and radiation pressure. (The wheel torque is implicit through  $\mathbf{h}_{k+1}$  in the above propagation scheme.) The environmental torques are computed in the RTSF using a detailed spacecraft model as well as accurate algorithms; in particular, the aerodynamic torque is computed using the FREEMAC algorithm (Reference 16), which generates velocity-dependent drag coefficients. We note, however, that the noise in SAMPEX wheel speed obscures the effects of the environmental torques. Thus, only  $N_{mag}$  is noticeable; this is given by  $N_{mag}=\boldsymbol{\mu} \times \mathbf{B}$ , where  $\boldsymbol{\mu}$  is the dipole moment of the MTA and  $\mathbf{B}$  is the magnetic field.

The differential equation for  $\mathbf{P}$  can be derived by noting that the error in  $\hat{\mathbf{X}}$  after propagation comes from two sources: (1) the error before propagation and (2) the random vectors,  $\boldsymbol{\eta}_{\omega}$  and  $\boldsymbol{\eta}_b$ , which are ignored in propagation. The linearized propagation equations for the errors follow as

$$\begin{aligned} \frac{d\mathbf{x}}{dt} &= \begin{bmatrix} -[\hat{\boldsymbol{\omega}} \times] & \mathbf{I}_{3 \times 3} \\ \mathbf{0}_{3 \times 3} & -\tau^{-1} \mathbf{I}_{3 \times 3} \end{bmatrix} \mathbf{x} + \begin{bmatrix} \boldsymbol{\eta}_{\omega} \\ \boldsymbol{\eta}_b \end{bmatrix} \\ &= \mathbf{F}(\hat{\boldsymbol{\omega}}) \mathbf{x} + \boldsymbol{\eta} \end{aligned} \quad (18)$$

Equation (18) defines  $\mathbf{F}$  and  $\boldsymbol{\eta}$ . Introducing  $\mathbf{Q}$ , the diagonal spectral density matrix of  $\boldsymbol{\eta}$ , through  $\langle \boldsymbol{\eta}(t) \boldsymbol{\eta}(t')^T \rangle = \mathbf{Q} \delta(t-t')$  it can then be shown (Reference 15) that the covariance matrix evolves according to

$$\frac{d\mathbf{P}}{dt} = \mathbf{F} \mathbf{P} + \mathbf{P} \mathbf{F}^T + \mathbf{Q} \quad (19)$$

Equation (19) is integrated numerically in the RTSF to obtain  $\mathbf{P}_{k+1}(-)$ .

### Updates Using Sensor Measurements:

Let  $V_B$  and  $V_I$  be the measured (body frame) and reference (GCI) vectors corresponding to a particular sensor and let  $\hat{V}_B = A(\hat{q}(-))V_I$ . The residual  $y$  is defined as  $y = V_B - \hat{V}_B$ . Linearizing the attitude errors about  $q_{true}$  yields

$$y = Hx(-) + \Delta V_B \quad (20)$$

where  $H = [-\hat{V}_B \times] 0_{3 \times 3}$  and  $\Delta V_B$  is random measurement error. The following optimality requirements can then be used to obtain the usual Kalman gain and covariance-update equations: (1) if the error is unbiased before a measurement ( $\langle x(-) \rangle = 0$ ), it should remain so after the update ( $\langle x(+) \rangle = 0$ ), and (2) the statistical average of the total error,  $\langle x(+)^T x(+) \rangle$ , should be a minimum:

$$K = P(-)H^T [HP(-)H^T + R]^{-1} \quad (21)$$

$$P(+) = [I_{6 \times 6} - KH]P(-)$$

where  $R = \langle \Delta V_B \Delta V_B^T \rangle$ . The correction  $x^*$  is then given by

$$x^* = Ky \quad (22)$$

for use in Equations (16) and (17). The covariance update in Equation (21) was chosen over more numerically stable algorithms due to memory and speed considerations on personal computers. To partially mitigate the risks,  $P(+)$  is symmetrized after the update. No adverse effects have been noticed to date.

For SAMPEX, no special treatment is necessary to construct  $R$  for the TAM, since independent magnetic field measurements are made along each body axis. The FSS, however, measures only two independent angles, and only the corresponding components of  $y$  are used in the computations. Details are given in Reference 5.

## 4. Tuning and Accuracy of the Rate Corrections

The telemetry digitization of the FSS is 0.5 deg; this value was used to construct  $R$  for FSS measurements. For the TAM, uncertainties in the reference magnetic field calculations are larger than the digitization errors of 0.3 mG; after the residuals were examined, a TAM noise of 3 mG was used to construct  $R$ .

A distinctive feature of telemetered SAMPEX data is the large wheel noise ( $\sim 1$  rad/sec). This noise yields torques of the order of  $10^{-2}$  N-m, far in excess of the maximum values of the environmental torques ( $\sim 10^{-6}$  N-m), and results in a noise of about  $1.7 \times 10^{-4}$  rad/sec in  $\omega_y$ . The pitch covariance  $P_{22}$  thus grows by about  $3 \times 10^{-8} (\Delta t)^2$  rad<sup>2</sup> between measurements. Since  $Q$  is the rate of change of  $P$  due to the process noise (Equations (19)),  $Q_{22}$  was correspondingly assigned a value of  $3 \times 10^{-8} \Delta t$  rad<sup>2</sup>/sec. To provide for the situation in which  $\omega_x$  and  $\omega_z$  are substantial (as during Sun acquisition), the same value was also assigned for  $Q_{11}$  and  $Q_{33}$ .

The discussion of Equations (8-11) then fixes the bottom three elements of  $Q$ , which correspond to  $\eta_b$ . Thus,  $p_{ii}$  in Equation (11) was chosen as  $3 \times 10^{-8}$  rad<sup>2</sup>/sec<sup>2</sup>, so that

$$Q_{ii} = \frac{6 \times 10^{-8}}{\tau} \frac{\text{rad}^2}{\text{sec}^3}, \quad i = 4, 5, 6$$

$\tau$  is chosen equal to the telemetry period: 0.5 sec for real-time data and 5.0 sec for playback data. As can be seen from Figure 1, the rate-error elements of  $P$  converge to the above value of  $p_{ii}$  very well.

Figure 2 clarifies the discussion of Equations (9) and (10), by examining the dependence of  $\tau$  on  $t_{upd}$ , the update period for  $\hat{b}$ . That is,  $\hat{b}$  is updated via Equation (17) only after every  $t_{upd}$  sec, as opposed to the telemetry period of 5 sec here. ( $\hat{q}$  is always updated every 5 sec.) Here "Sun angle" is the angle between the predicted and measured Sun vectors; thus, for a fixed set of measurements, larger Sun angles indicate larger propagation errors. Plots a and b show that, when  $\tau = t_{upd} = 5$ , the mean Sun angle is about 0.25 deg and rate corrections of the order of 10 deg/hour are estimated. In plots c and d,  $\tau$  is lowered to 1 sec while retaining the same value for  $p_{ii}$ . Thus,  $Q$  is now larger, and the RTSF does not correct for errors below this noise level. However, the mean Sun angle is now larger, about 1 deg, indicating that larger propagation errors arise if rates are not corrected. Plots e and f show the results for a larger value of  $\tau$ : 25 sec. If  $t_{upd}$  is retained at 5 sec (plot e), the RTSF quickly diverges and the Sun angle even reaches 180 deg. This happens

because  $\hat{b}$  does not decay to zero during the time between the updates, so that the updates,  $\hat{b}(+)$ , in Equation (9) also include past rate errors. The divergences are eliminated by choosing  $t_{\text{upd}} = 25$  sec, as shown in plot f. However, since  $\hat{b}$  is now updated infrequently, the Sun angles in plot f are generally larger than those in plot a.

The accuracy of the  $\hat{b}$  estimates was ascertained by using simulated data. These results are shown in Figure 3. In plot a, the truth model for  $\omega_y$  is noisy due to fluctuations in the inflight wheel data used to generate SIM722. The simulated data were input to the RTSF *but with a constant wheel speed equal to the value at 0 sec*, and we see that the RTSF's  $\omega_y$  estimates generally reflect the true mean values. However, significant differences occur around 100 and 450 sec, where changes in  $\omega_{\text{whl}}$  cause changes in the true  $\omega_y$ . This information is not available to the RTSF and leads to significant Sun angles, together with nonzero values for  $\hat{b}_y$  around these times in plot b. We see from plots a and b that the signs of these  $\hat{b}_y$  estimates agree with Equation (6). Quantitatively also, the  $\hat{b}_y$  estimates are reasonable; for example, the corrections total about 0.01 deg/sec during 0-200 sec, which compares well with the rate differences in plot a.

We thus see that tuning results confirm the arguments of Section 1 and that the rate corrections  $\hat{b}$  are accurate to 1 deg/hour.

## 5. Robustness of the RTSF Against A Priori Errors and Torque Errors

The RTSF was evaluated extensively with PB705 data where SAMPEX is in Sun acquisition soon after launch. The spacecraft is initially nutating rapidly— $\omega_y$  constant at about 0.3 deg/sec and  $\omega_x$  and  $\omega_z$  sinusoidal with amplitudes of about 0.6 deg/sec—before transitioning to the nominal 1-RPO mission mode. (The transition is clearly visible in Figure 10.) Thus, the Sun-acquisition part of PB705 is a rapidly varying situation and provides a stringent test of the RTSF's performance. In most results here, the RTSF was started with what we term *zero initial conditions*; i.e., the body frame is aligned with GCI and  $\omega = (0,0,0)$ .

Figure 4 shows the convergence of the RTSF results to single-frame solutions using both FSS and TAM data. Although the a priori errors are large—(-27, -91, 21) deg in attitude and (-0.5, 0.3, 0.4) deg/sec in the rates—the RTSF's estimates converge in about 300 sec. The effects of the a priori errors clearly show up in plot c, where  $\hat{b}$  is extremely large during convergence.

Figures 5 and 6 show another useful aspect of the RTSF: the ability to compensate for torque errors. Figure 5 shows results with PB705 during the transition to 1-RPO mode, with the TRIAD rates serving as the truth model. Here  $\omega_y$  drops from 0.3 deg/sec to the 1-RPO value of 0.06 deg/sec partly due to a substantial wheel torque. The wheel speeds input to the RTSF, however, were deliberately given the *wrong sign* during this run. Thus, around 200 sec, the RTSF's  $\omega_y$  estimate initially *increases*. This gives rise to large Sun angles, and significant  $\hat{b}_y$  are estimated (plot b) that eventually correct  $\omega_y$ ; the time lag needed to correct  $\hat{\omega}$  is finally eliminated in the 1-RPO mode where  $\omega_y$  is nearly constant. Similar results were, in fact, used during prelaunch tests of ground software to detect and rectify the conversion factor for telemetered wheel data.

Figure 6 presents results with PASS53 data where rate errors of about 1 deg/hour appear in phase with MTA activity. Unlike the data in Figure 5, the data here are unmodified, and the RTSF results suggest that the MTA needs to be calibrated.

Figure 7 presents results with PASS53 data highlighting the usefulness of estimating  $\hat{b}$  even in a slowly varying situation. Here propagation of  $\omega$  via Equation (4) was completely omitted, and the RTSF was run using zero initial conditions; the  $\omega_y$  estimate quickly converges to the 1-RPO value. In contrast, Figure 8 shows the results with PB705 data where the reverse situation holds: The a priori errors were small,  $\omega$  was propagated, but  $\hat{b}$  was not estimated. Large rate errors (which we ascribe to  $N_{\text{mag}}$  errors) accumulate over time and eventually degrade the attitude accuracy.

## 6. RTSF Advantages Over Single-Frame Algorithms

As mentioned in the introduction, a Kalman filter yields estimates via propagation of  $\hat{X}$  for state vector elements that are not observable. This is demonstrated here for two situations: (1) near-coalignment of the Sun and magnetic field vectors whereby the pitch angle is nearly unobservable and (2) attitude and rate estimation using only magnetic field data. (Note that Figure 3 is also a *magnetic-field-only* situation, since SIM722 models an eclipse.)

vectors whereby the pitch angle is nearly unobservable and (2) attitude and rate estimation using only magnetic field data. (Note that Figure 3 is also a *magnetic-field-only* situation, since SIM722 models an eclipse.)

Figure 9 presents the former case, with the top plot showing peaks of nearly 25 deg in both QUEST and TRIAD solutions for the pitch angle when the Sun-magnetic field angle falls below 5 deg. This occurs despite nominal values for all sensor and control data (not shown here) during this period. In contrast, the RTSF pitch estimates vary very little over the timespan, with these estimates now being generated using propagation alone. The absence of pitch observability does affect the RTSF pitch covariance  $P_{22}$ , whose growth due to  $Q$  in Equation (19) is not offset by measurements. Thus,  $P_{22}$  first rises steeply in plot b and then falls when the TAM data again provide useful information.

Figure 10 presents RTSF results using PB705 data but without using the available FSS data. The starting conditions here were the zero initial conditions as in Figure 4, but now attitude information is obtained through only the magnetic field  $B$ . Although a single measurement of  $B$  can yield only information regarding rotations perpendicular to it,  $B$  changes direction sufficiently during an orbit, so that all three attitude angles are observable over a sufficiently long span of data. This is indeed seen in Figure 10, where the RTSF's yaw angle estimates converge after about 1000 sec. After convergence, the RTSF attitude and rate estimates remain within 1.5 deg and 0.01 deg/sec, respectively, of the single-frame estimates (not apparent here). We attribute this difference to magnetic field model uncertainties since RTSF attitude accuracies of 0.1 deg were obtained using simulated data (Reference 7).

## 7. Robust TAM-Only Attitude and Rate Determination

Motivated by the successful TAM-only attitude-and-rate estimation by the RTSF (Figures 3 and 10), we have developed a robust TAM-only method that overcomes the following shortcomings of the RTSF: (1) Convergence of the RTSF estimates is not guaranteed since it is an extended Kalman filter, and (2) the TAM-only convergence is slow, about 1000 sec in Figure 10. These difficulties are overcome here by initializing the RTSF with the solution from the TAM-only deterministic algorithm (DA) of References 12 and 13.

The DA considers the following two time derivatives of the magnetic field  $B$ : the one in the reference frame,  $\dot{B}_R$ , and the one in the body frame,  $\dot{B}_A$ . (The notation used here conforms with that of References 12 and 13.) They are related formally by the vector equation:

$$\dot{B}_R = \dot{B}_A + \omega \times B \quad (23)$$

Noting that  $|B|$  is invariant under orthogonal transformations, two special orthogonal axes perpendicular to  $B$  (Reference 12) can be chosen such that the projections  $\omega_2$  and  $\omega_3$  of  $\omega$  along these axes are restricted to lie on a circle. The DA then extracts the radius and center of this circle from TAM data.

The constraint on  $\omega_2$  and  $\omega_3$  can be parameterized by an angle  $\Phi$  so that  $\omega$  is described by two unknown parameters:  $\omega_1$ , the projection of  $\omega$  onto  $B$ , and  $\Phi$ . These are then determined using  $\dot{\omega}$  and the second time derivatives of  $B$  as evaluated in the two frames. From Equation (4),  $\dot{\omega}$  is expressed as a function of  $\omega$  and  $N_{tor}$ , yielding

$$\Lambda_0(\Phi) + \omega_1 \Lambda_1(\Phi) + \omega_1^2 \Lambda_2(\Phi) = 0 \quad (24)$$

where the vectors  $\Lambda_k(\Phi)$ ,  $k = 0, 1, 2$ , are defined in Reference 13. Projecting Equation (24) onto the plane perpendicular to  $B$  yields two transcendental equations for  $\Phi$  and  $\omega_1$ , generally yielding at least two solutions. The ambiguity in the solutions can be removed if  $N_{tor}$  can be neglected, so that we can demand that the reference frame components of the angular momentum  $L$  be constant. For SAMPEX, in particular, this requirement holds during eclipses when there is no magnetic control.

The efficacy of the DA calculations was tested using eclipse data from PB722, and evaluating  $\dot{B}_R$  and  $\dot{B}_A$  using 100-sec batches of TAM data. Figure 11 presents attitude and rate results from this calculation, using a 2-3-2 Euler sequence to parameterize the attitude. The advantage of this parameterization is that the third Euler angle directly reflects the 1-RPO rate of the spacecraft, whereas the other two angles are very nearly constant for small nutational amplitudes. We see that, although up to four solutions appear toward the middle of the timespan, only two solutions appear toward the extremities. Demanding the constancy of  $L$  in the reference frame then unambiguously selects the correct solution

To understand why we usually have only two solutions, it is useful to approximate  $L \approx h$ , which holds very well for SAMPEX. Then

$$\dot{\omega}(\Phi, \omega_1) = \Omega_0^0(\Phi) + \omega_1 \Omega_1^0 \quad (25)$$

where  $\Omega_0^0(\Phi) = -I^{-1}[\omega_1(\Phi) \times h]$ ,  $\Omega_1^0 |B| = -I^{-1}[B \times h]$ , and  $\omega_1$  denotes the projection of the  $\omega$  onto the plane perpendicular to  $B$ . This linearizes Equation (24) and yields:

$$\Lambda_0(\Phi) + \omega_1 \Lambda_1(\Phi) = 0 \quad (26)$$

One can then exclude  $\omega_1$  by projecting these equations onto the vector  $C_3^T |B| = B \times \Lambda_1(\Phi)$ . This leads to a quadratic equation with respect to  $x = \tan(\Phi/2)$ , analogous to that in Reference 12 for the constant- $\omega$  limit. (The quadratic equation turns into Equation (3-11) in Reference 12 if one sets  $h = 0$ .)

The DA yields multiple solutions when  $B$  is approximately antiparallel to the roll axis. Since  $h$  for SAMPEX is directed along the pitch axis,  $\Omega_0^0(\Phi)$  is approximately antiparallel to  $B$  for any value of  $\Phi$ . Contributions to  $\Omega_0^0(\Phi)$  cannot then be neglected in  $B \times \dot{\omega}$ , and this gives rise to the multiple solutions, at about 600 sec in Figure 11.

Figure 12 compares the RTSF roll angle results obtained by initializing the filter with two different schemes: (1) zero initial conditions and (2) with the correct DA solution from Figure 11. It is evident that using the DA for initialization significantly improves the attitude accuracy by reducing the convergence time of the RTSF. Note that results with both initial conditions reflect oscillations with the spacecraft's nutational period ( $\approx 120$  sec). To illustrate the importance of the initial conditions, we note that the RTSF solutions diverged when the spurious solution of Figure 11 was used to initialize the filter. In this context the successful convergence with zero initial conditions is also noteworthy. (The large nutational amplitudes for zero initial conditions are eventually damped by the RTSF's rate corrections.)

## 8. Conclusions

We find that the SAMPEX RTSF's method of estimating the rate errors  $b$  that accumulated during the period between rate updates yields accurate results while minimizing the computational load. The tuning scheme, which exploited the relationship between the converged covariances, noise characteristics of SAMPEX data, and the Markov time constant, was simple but effective, and resulted in estimates of  $b$  accurate to 0.0003 deg/sec (1 deg/hour). Consequently, estimating  $b$  significantly enhanced the performance of the SAMPEX RTSF by providing robustness against

- Large a priori attitude and rate errors
- Errors in the control torques

In fact, we see that rates were generated accurately in slowly varying situations even when the Euler equation is not used.

The RTSF's advantages over single-frame algorithms were demonstrated through

- Stability of pitch angle estimates during Sun-magnetic field near-coalignment, where both QUEST and TRIAD solutions were incorrect by nearly 25 deg
- Magnetic-field-only attitude and rate determination to within 1.5 deg and 0.01 deg/sec of the single-frame solutions using zero initial conditions

The deterministic magnetic-field-only algorithm significantly enhanced the robustness and accuracy of the filter by generating coarse estimates of the a priori attitude and rates. This results in an important contingency algorithm for spacecraft like SAMPEX which have no sensor redundancy.

## References

1. J. S. Wertz (ed.), *Spacecraft Attitude Determination and Control*, D. Reidel Publishing Co., Dordrecht, Holland, 1984
2. E. Harvie and D. Chu, "Dynamics Modelling for ERBS Attitude Propagation," Proceedings of Third International Symposium on Spacecraft Flight Dynamics, European Space Agency Conference Publication No. ESA-ST 326, Darmstadt, Germany, December 1991
3. M. D. Shuster and S. D. Oh, "Three-Axis Attitude Determination from Vector Observations," *Journal of Guidance and Control*, Vol. 4, p. 70-77, 1981
4. NASA Goddard Space Flight Center (GSFC), Flight Dynamics Division, 554-FDD-91/145, *Solar, Anomalous, and Magnetospheric Particle Explorer (SAMPEX) Real-Time Attitude Determination System for Personal Computer (SRTADS/PC) Specifications Document*, P. Crouse (GSFC), September 1991
5. NASA Goddard Space Flight Center, Flight Dynamics Division, 553-FDD-93/024R0UD0, *Solar, Anomalous, and Magnetospheric Particle Explorer (SAMPEX) Real Time Sequential Filter (RTSF): Evaluation Report*, M. Challa (CSC), prepared by Computer Sciences Corporation, April 1993
6. NASA Goddard Space Flight Center, Flight Dynamics Division, FDD-554-91/030, *Real Time Sequential Filter (RTSF) Mathematical Model for Dynamic Propagation of Angular Rates*, M. Challa (CSC) and M. Rokni (CSC), prepared by Computer Sciences Corporation, January 1991
7. NASA Goddard Space Flight Center, Flight Dynamics Division, 553-FDD-93/076R0UD0, *Attitude Dynamics Task: Attitude Determination Using Only Magnetometer Data for the Solar, Anomalous, and Magnetospheric Particle Explorer (SAMPEX)*, G. Natanson (CSC), M. Challa (CSC), S. Kotaru (CSC), and C. Woodruff (CSC), prepared by Computer Sciences Corporation, August 1993
8. E. J. Lefferts, F. L. Markley, and M. D. Shuster, "Kalman Filtering for Spacecraft Attitude Estimation," *Journal of Guidance, Control, and Dynamics*, Vol. 5, No. 5, Sept.-Oct. 1982, pp. 417-429
9. J. Deutschmann, I. Y. Bar-Itzhack, and M. Rokni, "Comparison and Testing of Extended Kalman Filters for Attitude and Estimation of the Earth Radiation Budget Satellite," Flight Mechanics and Estimation Theory Symposium, NASA Conference Publication 3102, Greenbelt, MD, May 1990
10. J. Sedlak and D. Chu, "Kalman Filter Formulation of Attitude and Gyro Bias with the QUEST Observation Model," Paper No. AAS 93-297, Proceedings of the AAS/GSFC International Symposium on Space Flight Dynamics, NASA Goddard Space Flight Center, Greenbelt, MD, April 1993
11. R. Hammon, "An Application of Random Process Theory to Gyro Drift Analysis," *IRE Transactions on Aerospace and Navigational Electronics*, Vol. 7, pp. 84-91, September 1960
12. G. A. Natanson, S. F. McLaughlin, and R. C. Nicklas, "A Method of Determining Attitude From Magnetometer Data Only," Flight Mechanics and Estimation Theory Symposium, NASA Goddard Space Flight Center, Greenbelt MD, May 1990
13. G. A. Natanson, "A Deterministic Method for Estimating Attitude From Magnetometer Data Only," Paper No. IAF-92-0036, Proceedings of the World Space Congress, Washington DC, August-September 1992
14. J. K. Forden, T. W. Flatley, D. A. Henretty, and E. G. Lightsey, "On-board Attitude Determination and Control Algorithms for SAMPEX," Flight Mechanics and Estimation Theory Symposium, NASA Conference Publication 3102, May 1990
15. A. Gelb (ed.), *Applied Optimal Estimation*, The MIT Press, Cambridge, Massachusetts, 1974
16. D. C. Folta and D. F. Baker, *Increased Ephemeris Accuracy Using Attitude-dependent Aerodynamic Force Coefficients for Inertially Stabilized Spacecraft*, Flight Mechanics and Estimation Theory Symposium, NASA Conference Publication No. 3123, May 1991

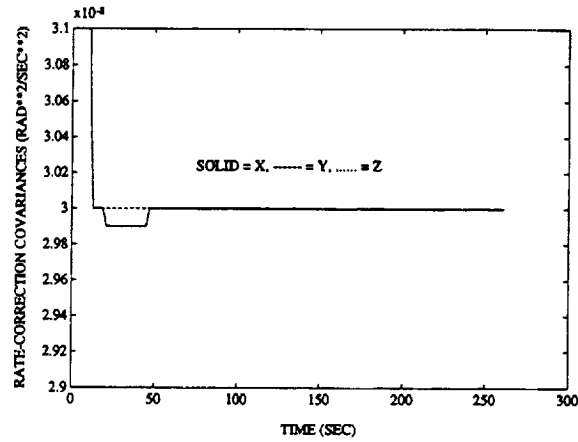
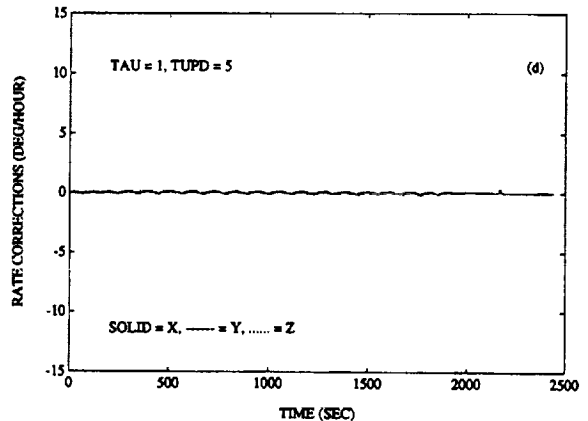
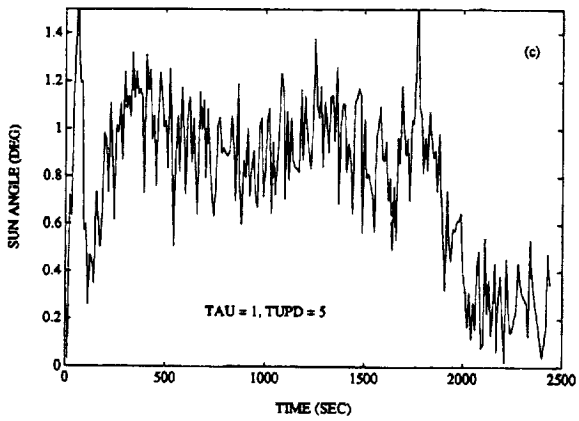
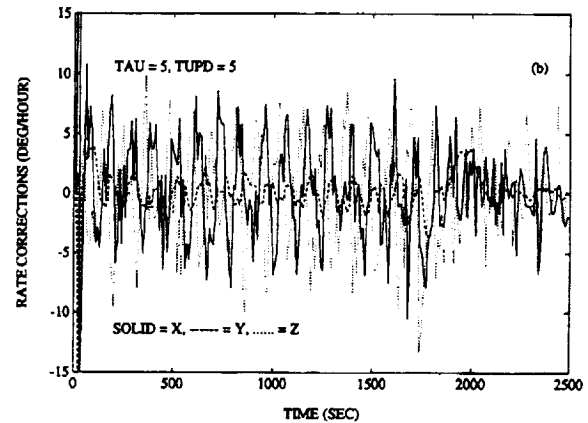
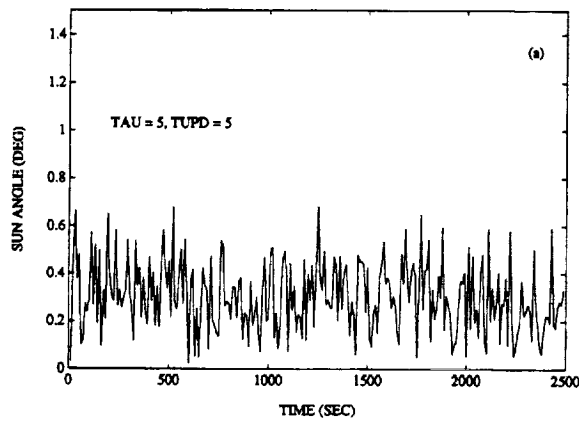
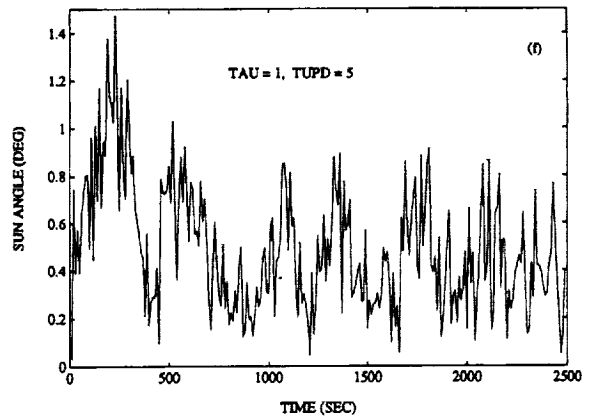
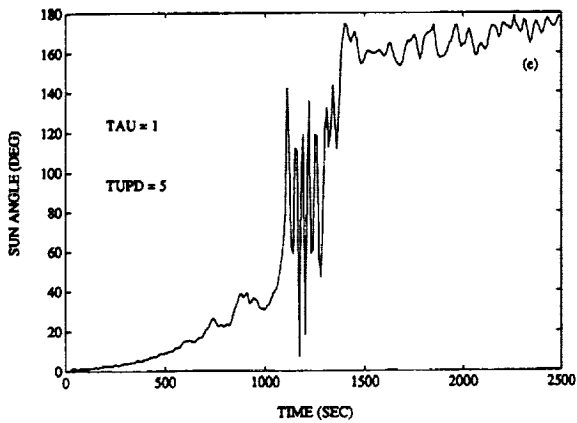


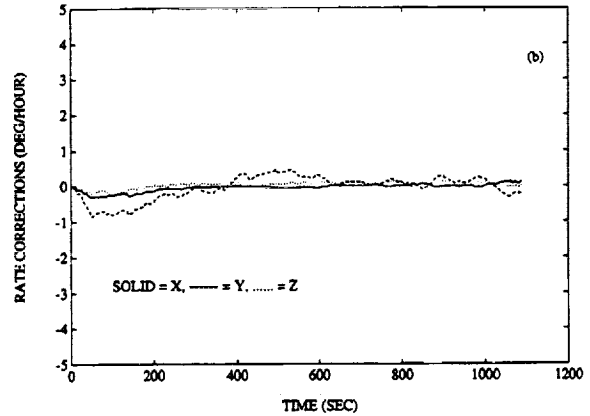
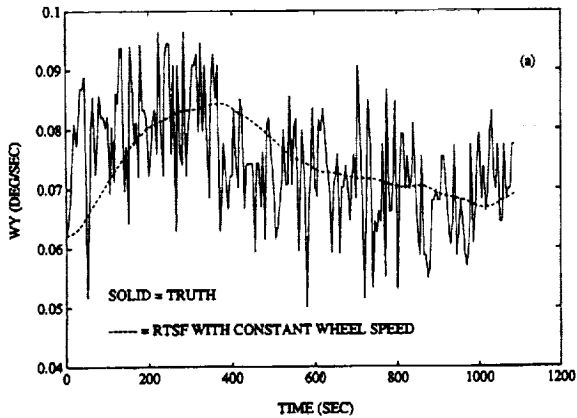
Figure 1. Results Using PB705 Data Showing Convergence of Rate Correction Covariances to the Theoretical Value



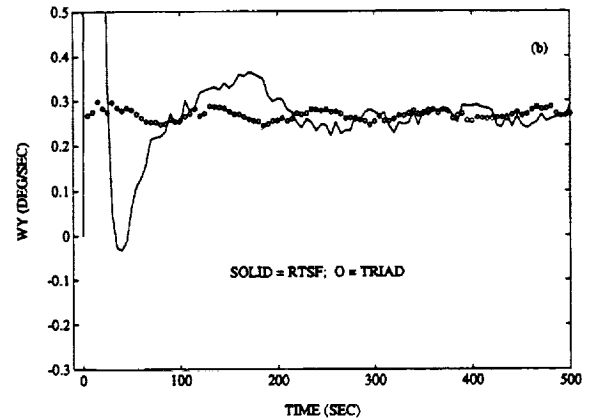
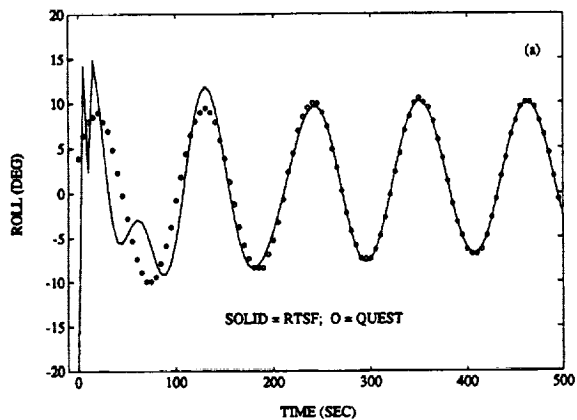
Figures 2a-2d. RTSF Results Using PB705 Data Showing That Tuning is Optimal When Both  $\tau$  and  $t_{upd}$  Equal the Telemetry Period of 5 sec



**Figures 2e and 2f. RTSF Results Using PB705 Data Showing That Tuning is Optimal When Both  $\tau$  and  $t_{upd}$  Equal the Telemetry Period of 5 Sec**



**Figures 3a and 3b. Results Using SIM722 Data Showing Accuracy of the Rate Corrections**



**Figures 4a and 4b. Results Using PB705 Data Showing Convergence of RTSF Estimates to Single-Frame Results Despite Large a Priori Errors**

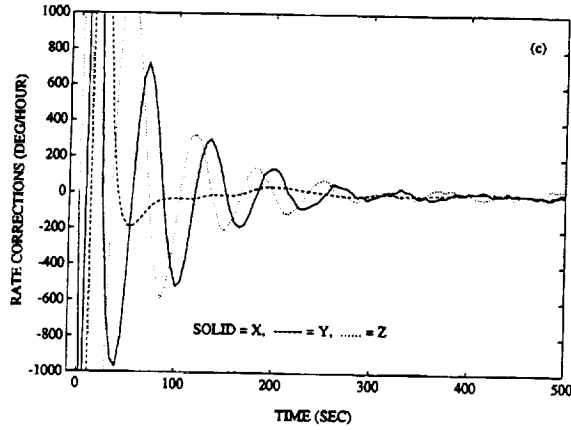
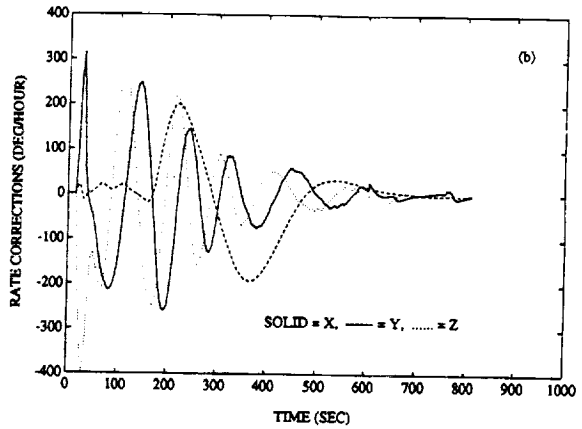
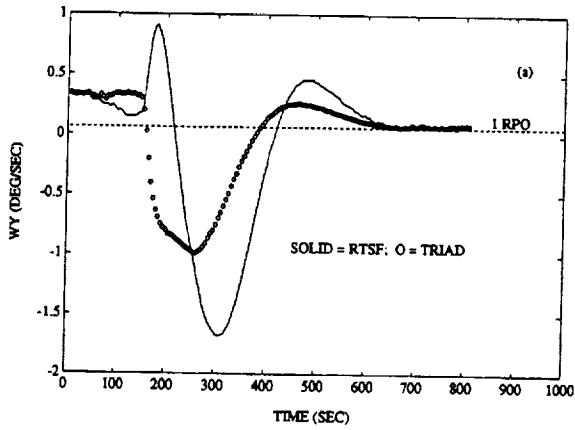
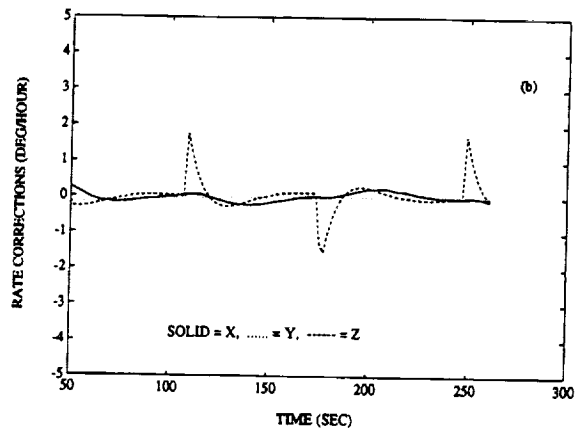
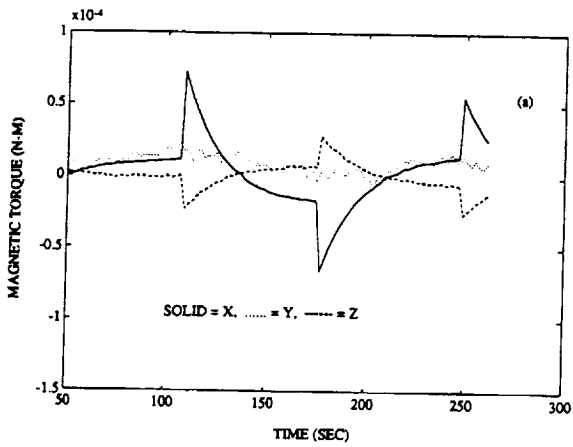


**Figure 4c. Results Using PB705 Data Showing Convergence of RTSF Estimates to Single-Frame Results Despite Large a Priori Errors**



**Figures 5a and 5b. Compensation by the Rate Corrections for Wheel Torque Errors in Modified PB705 Data**



**Figures 6a and 6b. Results Using PASS53 Data Suggesting Errors in Magnetic Control Torques**

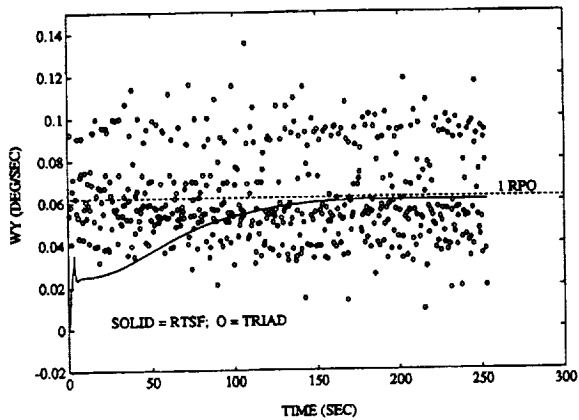


**Figure 7. Results Using PASS53 Data Showing Robustness of RTSF When Rate Propagation Is Suppressed**

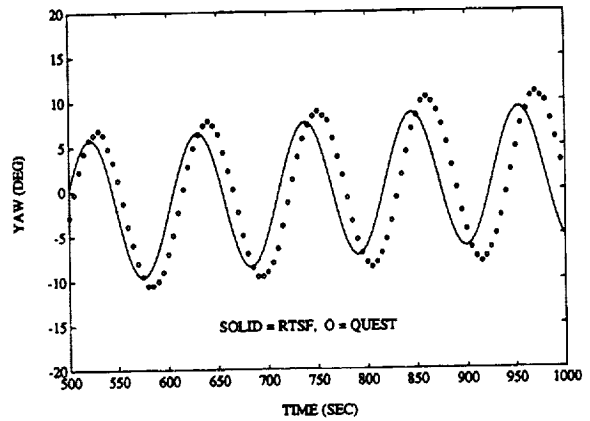


**Figure 8. Results Using PB705 Data Showing Significant RTSF Errors When Rate Corrections Are Not Estimated**

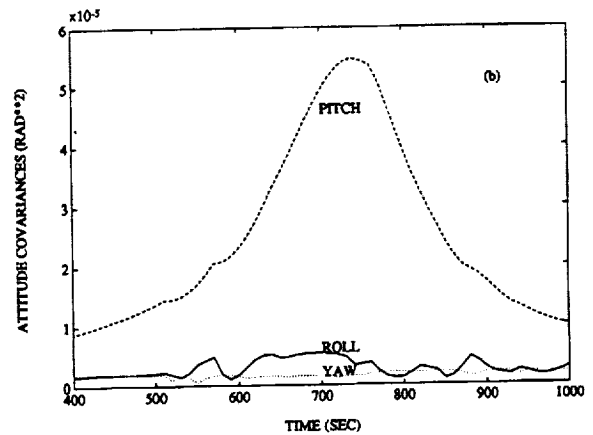
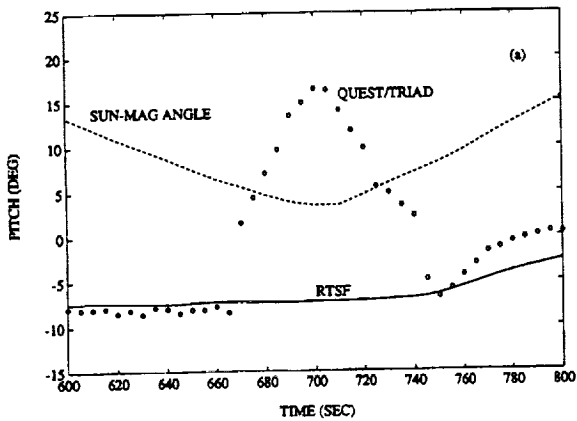
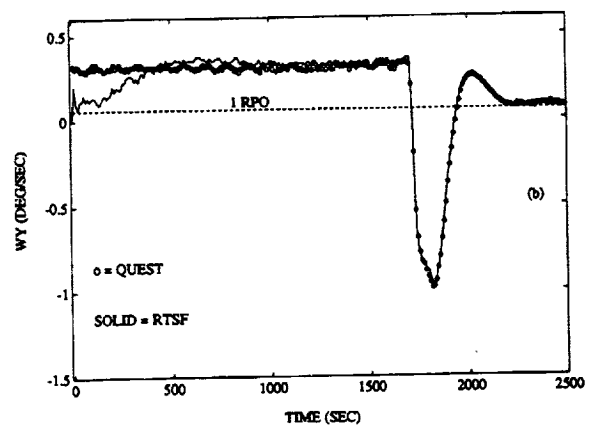
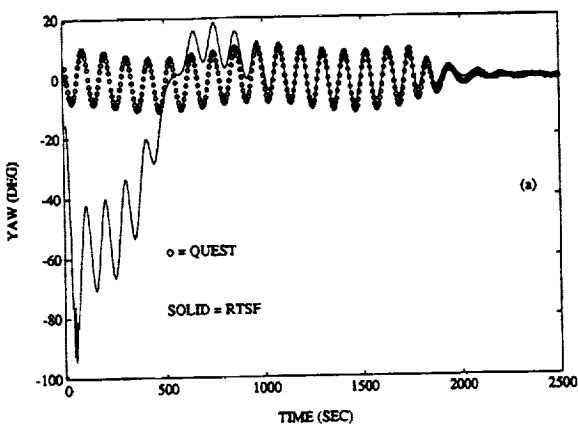
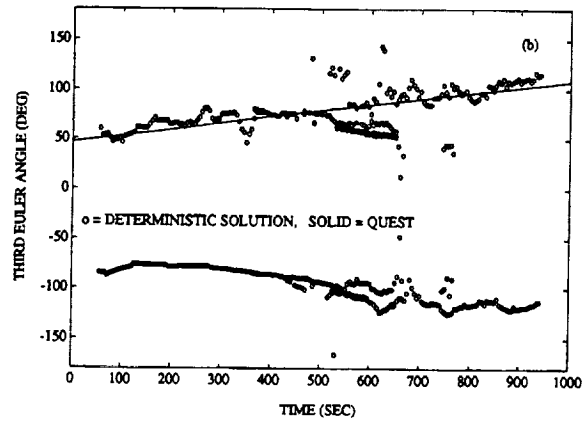
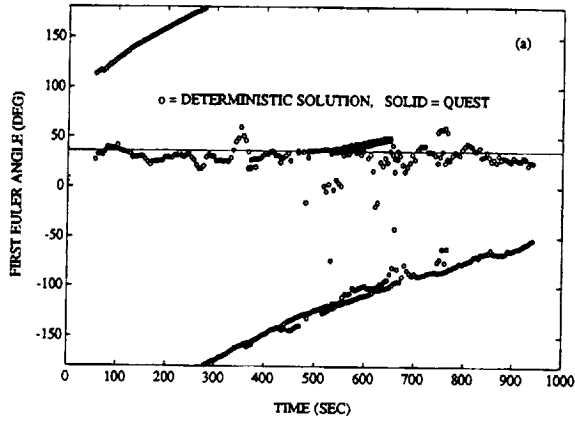


**Figure 9a and 9b. Results Using PB825 Data Showing Robustness of RTSF During Near-Coalignment of Sun and Magnetic Field Vectors**



**Figures 10a and 10b. Convergence of RTSF Estimates for PB705 Data When Only TAM Data and Large a Priori Errors Are Used**



**Figures 11a and 11b. TAM-Only Attitude and Rate Solutions Generated by the Deterministic Method During an Eclipse in PB722 Data**

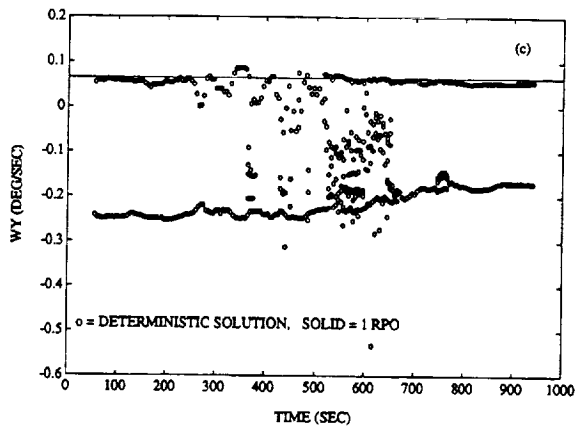


**Figure 11c. TAM-Only Attitude and Rate Solutions Generated by the Deterministic Method During an Eclipse in PB722 Data**

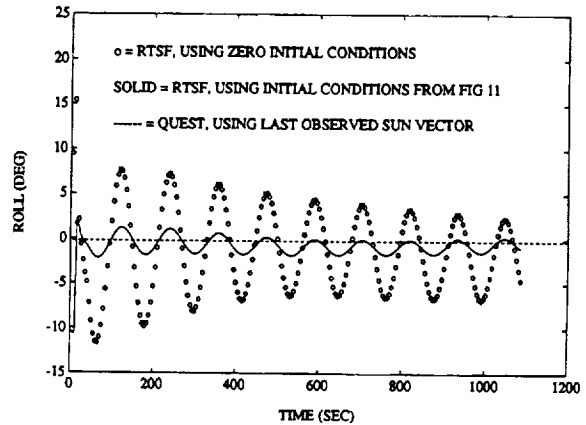


**Figure 12. RTSF TAM-Only Results for PB722 Data Showing Faster Convergence Using the Correct Solutions of Figure 11**

